Excitable Actin Dynamics in Lamellipodial Protrusion and Retraction

Gillian L. Ryan,[†] Heather M. Petroccia,[†‡] Naoki Watanabe,[§] and Dimitrios Vavylonis[†]

[†]Department of Physics, Lehigh University, Bethlehem, Pennsylvania; [‡]Department of Physics, Villanova University, Villanova, Pennsylvania; and [§] Laboratory of Single-Molecule Cell Biology, Tohoku University Graduate School of Life Sciences, Sendai, Miyagi, Japan

SUPPORTING MATERIAL

1. Materials and Methods

Live Cell Imaging

Live cell imaging was carried out as described in (1). XTC cells transiently expressing EGFP- and mCherry-tagged proteins were trypsinized and allowed to spread on a poly-L-lysine (PLL)-coated glass coverslip in 70% L-15 medium without serum. Some cells were stimulated by addition of FCS, as indicated. The flow cell was then placed on the stage of Olympus BX51 microscope equipped with Cascade II:512 (Roper Scientific) or BX52 microscope equipped with CoolSNAP HQ (Roper Scientific). A restricted area near the cell edge was illuminated using a 75 W xenon illumination system. Imaging acquisition was carried out at 21-23 °C using the Metamorph software (Molecular Devices) and an Olympus oil objective, PlanApo 100× (NA 1.40). Under the experimental conditions described, most of cells form flat, well-spread lamellipodia and we chose cells without ruffles for analysis. The body of the cell did not move significantly during the analysis.

Measurements of Protrusion Rate and Intensity

The leading edges of cells expressing fluorescent proteins were tracked over time by modifying JFilament (2). Active contours were fit to the intensity gradient between the interior and exterior of the cell at the leading edge. The software allowed for the semi-automated tracking of the leading edge by evolving the contour from the previous time point. Manual interaction allowed correction of tracking failures. We selected cells that were well-spread and near-circular in shape in order to convert the contours to polar coordinates at 1-degree intervals, see Fig. 1 *E* (3). When only a fraction of a cell was visible, we estimated the position of the cell center. The normal leading edge velocity was calculated at each angle as the change in radial distance of the leading edge from the cell center. To measure the local intensity of fluorescent proteins along the cells' leading edges, we generated a ribbon of leading edge (see Fig. 1 *F*). We integrated the intensity within the ribbon to get the total intensity as a function of angle.

Measurements of Retrograde Flow

To measure retrograde flow we performed fluorescent single molecule fluorescence microscopy experiments, sampling at 1 s intervals. Individual speckles were tracked using Speckle TrackerJ (4). Measurements were reproducible by an independent user. The measurements produced x- and y-coordinates for each speckle over time (See. Fig. S1 *A*). Speckle velocities were calculated by calculating the local line of best fit to both the x- and y-coordinates of the trajectories over 20 s intervals. In Fig. S1, the average error in the x- and y-velocity of these fits was 2.7 nm/s, being smaller than 4 nm/s for 93% of the fits. The standard deviation of measured speckle position from lines of best fit were 0.06 pixels in the x-direction, and 0.08 pixels in the y-direction (1 pixel = 80 nm). This approaches the limit of our spatial resolution: when measuring immobile EGFP speckles stuck to the glass outside the cell we found standard deviations in the x- and y– positions over time of 0.02-0.13 pixels. Speckle lifetimes sample a large distribution (1, 5). We did not calculate velocities for speckles with lifetimes less than 20 s.

To correlate retrograde flow with leading edge speed, the leading edge was tracked with JFilament. Since the leading edge is difficult to detect in cells expressing low levels of fluorescent labels, the movie that was tracked with JFilament was first time-averaged, so that each frame was a moving average of 20 frames (an interval smaller than the typical period of protrusion/retraction cycles). This averaging enhanced contrast at the leading edge. For the speckle data, we calculated the protrusion velocity of the leading edge using a moving average over 40 s. The intersection of a linear fit of the total speckle trajectory and the active contour at the leading edge identified the leading edge position to which the speckle corresponded.

Correlation Analysis

Cross-correlation coefficients between $f(t,s)$ and $g(t,s)$, c_{f*g}, were calculated as a function of time interval Δt and arc-length distance Δs using:

$$c_{f*g}(\Delta t, \Delta s) = \sum_{t=1}^{N} \sum_{s=1}^{M} \frac{(f(t,s)-\bar{f})(g(t-\Delta t, s-\Delta s)-\bar{g})}{(N-1)(M-1)\sigma_f \sigma_g}, \tag{S1}$$

where f and g are the quantities being correlated. N denotes the number of time points and M the number of positions. $\bar{f}$ and $\bar{g}$ are averages of the functions and σ_f and σ_g indicate standard deviations of f and g, respectively. Auto-correlation functions used identical f and g.

Computer Simulation

Simulations were run in one dimension along a line of size L (see table S1), representing the arc-length of the cell, with periodic boundary conditions. The model was solved by integrating the partial differential equations numerically, using a fourth order Runge-Kutta method. The value of the noise term was selected from a Gaussian probability distribution with zero mean and width $s_0/\sqrt{dx\,dt}$, where dt = 0.005 s is the integration time step. The lattice spacing is $dx = 5\sqrt{2dtD_A}$. The system was relaxed for a minimum of 2000 s before data was taken.

2. Choice of Non-linear Terms and Dependence of System Behavior on Parameter Values.

2.1 Choice of Non-linear Terms

We modeled the negative feedback in Eqs. (1) and (4) using an exponential cutoff, $e^{-\frac{F}{F_S}}$. This term prevents F-actin from accumulating in amounts that far exceed F_S. Excitations away from steady state are driven by the autocatalytic term $\rho(B) = r_0 + r_2 B^2$ in Eq. (4). As explained below, we chose a quadratic form because it is a simple non-linear function that is adequate to reproduce the observed phenomena. During an excitation, the concentration of actin near the leading edge approximately doubles (see Fig. 1 and 4). Given the rate constants of Table S1 and a period of ~150 s, we anticipate a change of similar magnitude in the concentration of free barbed ends. Now the term $\rho(B)e^{-\frac{F}{F_S}}$ should have approximately the same value at both steady state, $B = B^*$ and $F = F^*$ and at the instant in time when the free barbed end concentration is at a maximum, $B \approx 2B^*$ and $F = \alpha F^*$. Since B and F are out of phase, we estimate $1.1 < \alpha < 1.5$. It is easy to show that, assuming a power law, $\rho(B) \sim B^n$, would require $2 \lesssim n \lesssim 5$. For the work presented here we chose the smallest integer exponent consistent with this requirement. We also include a constant term, r_0 in $\rho(B)$ to prevent unphysical fixed points with very small concentrations of free barbed ends.

2.2 Choice of Parameters and Linear Stability Analysis

We display model parameter values in Table S1. In choosing model parameters, we used numbers from experiments when possible. For example, k_F^+ and k_F^- were taken from experiment. This left four undetermined rate constants. We used four constraints to calculate their values. One of the constraints was that the resulting average concentration of F-actin is ~ 1000 µM (6-8). The concentration of free barbed ends within a band of width d ~ 2 µm near the leading edge is approximately 1 µM (1). In the model, which does not distinguish distance from the leading edge, this corresponds to a barbed end concentration 1 µM × d/w = 0.4 µM, where w ~ 5 µm is the width of the lamellipodium. Thus, a second condition was that the average value of the barbed end concentration is ~ 0.4 µM. The third condition was that the system is in a region of parameter space in which relaxation to steady state occurs with underdamped oscillations. The fourth condition was that the period of the oscillations is ~ 130 sec, as observed experimentally. Finally, the diffusion coefficient of the activator was selected to match the width of the spatial correlation function in Fig. 2 *B*. In the following two subsections we describe how we selected parameters using the above constraints and linear stability analysis.

2.2.1 Linear Stability Analysis

In this section we perform stability analysis of the model described by Eq. (1) and (4) of the main text, without the noise term:

$$\frac{\partial B}{\partial t} = (r_0 + r_2 B^2)e^{-\frac{F}{F_S}} - k_A^- B + D_A \nabla^2 B, \tag{S2}$$

$$\frac{\partial F}{\partial t} = k_F^+ B - k_F^- F. \tag{S3}$$

We used linear stability analysis to calculate the stability of the steady-state solutions. We show that parameters can be chosen such that the system is in a stable region, close to the boundary of an unstable region. The addition of a noise term in Eq. (S1) then transiently perturbs the stable state of the system, generating spontaneous excitations.

Stability analysis is performed around a homogeneous steady state $B=B^*$ and $F=F^*$. Fixed points B^* and F^* are defined by the nullclines of a homogeneous system (i.e. no dependence on arc length distance) $u(B^*,F^*)=v(B^*,F^*)=0$, where

$$u(B,F) = (\,r_0 + \,r_2B^2)\,e^{-\frac{F}{F_s}} - k_A^- B, \tag{S4}$$

$$v(B,F) = k_F^+ B - k_F^- F, \tag{S5}$$

While Eqs. (S4) and (S5) can have up to 3 fixed points, for parameter values near those of Table 1, there is a single fixed point, see Fig. S6.

Defining $b(x,t) = B(x,t) - B^*$ and $f(x,t) = F(x,t) - F^*$, considering sufficiently small deviations from the fixed point, and Fourier transforming $x \rightarrow q$, we obtain from Eqs. (S1) and (S2):

$$\begin{pmatrix} \dot{b}_q \\ \dot{f}_q \end{pmatrix} = J \begin{pmatrix} b_q \\ f_q \end{pmatrix}, \quad \text{where} \quad J = \begin{bmatrix} 2r_2B^* e^{-F^*/F_s} - (k_A^- + D_A q^2) & \dfrac{-\left(r_0 + r_2 B^{*2}\right)}{F_s} e^{-F^*/F_s} \\ k_F^+ & -k_F^- \end{bmatrix}. \tag{S9}$$

Here, J is the Jacobian matrix. The characteristic equation for this system is $\lambda^2 - TrJ\lambda + \det J = 0$. Solving this for λ we get two wave-number dependent eigenvalues of the form $\lambda(q) = \lambda'(q) + i\lambda''(q)$. We may use these eigenvalues to distinguish between parameter sets based on the type of behaviors they elicit within the model. We separate these into three distinct cases: (I) both eigenvalues real, (II) both eigenvalues complex with negative real part that give unstable solutions to the linearized equation, and (III) both eigenvalues complex with positive real part that generate stable solutions.

Case I. Two real eigenvalues occur when $\lambda''(q) = 0$. This requires that $\det J < \frac{(TrJ)^2}{4}$,or

$$-\left(2r_2B^* e^{-F^*/F_s} - (k_A^- + D_A q^2)\right)k_F^- + \left(\frac{\left(r_0 + r_2B^{*2}\right)}{F_s} e^{-F^*/F_s}\right)k_F^+ < \frac{1}{4}\left(2r_2B^* e^{-F^*/F_s} - (k_A^- + D_A q^2) - k_F^-\right) \tag{S10}$$

Real λ indicate stable or unstable fixed points, depending on the sign of λ. Since we search for systems with excitable behavior, we do not search for parameter values in this region.

Case II. Two complex eigenvalues result from parameter sets in which

$$-\left(2r_2B^* e^{-F^*/F_s} - (k_A^- + D_A q^2)\right)k_F^- + \left(\frac{\left(r_0 + r_2B^{*2}\right)}{F_s} e^{-F^*/F_s}\right)k_F^+ > \frac{1}{4}\left(2r_2B^* e^{-F^*/F_s} - (k_A^- + D_A q^2) - k_F^-\right) \tag{S11}$$

The real component of both eigenvalues is negative when $TrJ < 0$, or, equivalently

$$B^* e^{-F^*/F_s} < \frac{k_A^- + D_A q^2 + k_F^-}{2r_2}\ . \tag{S12}$$

A system fulfilling (S10) and (S11) will have an unstable fixed point. However, because the system of equations (S1) and (S2) gives bounded solutions, this indicates that the solution would evolve into a limit cycle, in which the system would produce oscillatory behavior. The period of these oscillations, estimated from the linear stability analysis is $\tau = 2\pi/Im(\lambda)$.

<u>Case III.</u> Here, condition in Eq. (S10) is fulfilled, but the real component of the eigenvalues is positive, or $TrJ > 0$:

$$B^* e^{-F^*/F_s} > \frac{k_A^- + D_A q^2 + k_F^-}{2r_2} \quad . \tag{S13}$$

A system fulfilling Eq. (S10) and (S12) will have a stable solution at its fixed point. If perturbed, such a system will relax back to the stable solution in an oscillatory manner. The predicted period of the oscillations in this case is $\tau = 2\pi/Im(\lambda)$. The relaxation rate is described by the dimensionless damping ratio $\zeta = TrJ/2\sqrt{detJ}$ (here $\zeta > 1$ is overdamped, $\zeta < 1$ is underdamped, and $\zeta = 0$ is undamped).

2.2.2. Selection of Parameter Values using Linear Stability Analysis

We used experimental values to estimate many of the rate constants in Table 1. In selecting values for the four unknown rate constants r_2 and r_0, F_s, and k_A^- , we required the system to satisfy the following four conditions (i) have a fixed point with $B^* \approx 0.4$ μM, (ii) have a fixed point with $F^* \approx 1500$ μM, (iii) the $q = 0$ case of the linear stability analysis lies in a type III region, but not far from a type II region such that the damping ratio is sufficiently small $\zeta \approx 0.25$ (to get excitable behavior with only moderate damping), and (iv) the period τ is approximately 130 sec, as observed experimentally.

Fig. S7 *A* and *B* shows linear stability diagrams for $q = 0$ as a function of two model parameters, k^-_A and k^-_F, and r_0 and r_2, respectively. Stars indicate the parameter set of Table I, for which the system belongs to Case III and has fixed point close to $B^* \approx 0.4$ μM, $F^* \approx 1500$ μM.

Fig. S7 *C* and *D* display the damping ratio ζ as a function of the same parameters as in Fig. S7 *A* and *B*, for $q = 0$ (ζ is only plotted for Case III). The damping ratio approaches zero close to the region of Case II. The values of k_A^- and k_F^- must both exceed a threshold for ζ to become sufficiently low. The value of r_2 must exceed an r_0-dependent threshold for ζ to become sufficiently low. The point corresponding to Table I has $\zeta \approx 0.25$, as required.

Fig. S7 *E* and *F* display the period τ as a function of the same parameters as in Fig. S7 *A* and *B*, for $q = 0$. The period of oscillation is sensitive to changes in the off-rates k_A^- and k_F^-, with a range $\tau = 25$-500 s depicted. Either of k_A^- and k_F^- must be sufficiently low for large τ to be around 130 s. The period is less sensitive to changes in r_2. It is within a range 130-220 s for the values of r_0 shown in the figure. The point corresponding to Table 1 has period $\tau \approx 130$ s, which was observed experimentally.

Finally, to select the value of the diffusion coefficient of the activator, D_A, we required that the damping ratio $\zeta(q)$ increases to ~ 1 at a wavenumber $q \approx 1$ μm^{-1}. $D_A = 0.1$ μm^2/s fulfills this and reproduces a width for the spatial correlation function similar to that in Fig. 2 *B* (full-width-half maximum approximately 5.2 µm). A decrease to D_A = 0.05 µm^2/s results in a full-width-half-maximum of 3.4 µm, while an increase to D_A = 0.4 µm^2/s results in a full-width-half-maximum of 8.8 µm. The effect of varying q with fixed D_A is shown in in Fig. S8. We find that increasing the value of q leads to shrinkage of the unstable region II (see Fig. S8 *A* and *B*). We also find that short wavelengths are more strongly damped compared to longer wavelengths. This is evident from the increase of the damping ratio with increase in wavenumber, shown in Fig. S8 *C*. For the parameters in Table 1, we find that the system switches from an underdamped regime (Case III) to an overdamped case (Case I) at a wavenumber q = 0.97µm^{-1} (oscillatory solutions are not possible for wavenumbers above this value of q). This is further evidenced by examining the dependence of the period τ on q (Fig. S8 *D*). The period is approximately constant for low values of q but diverges as $q \to 0.97$ µm^{-1}, indicating that oscillatory solutions are not possible for smaller wavelengths.

3. Arp2/3 Complex as Indicator of Activator Mechanism

Here, we explore the relationship of Arp2/3 complex concentration with the concentration of barbed ends, *B*, and F-actin, *F*, in the model of Eqs. (1)-(4) of the main text. We specifically examine the expected behavior of the Arp2/3 complex concentration assuming that the Arp2/3 complex accumulates at a rate proportional to the activator concentration (i.e. the Arp2/3 complex is downstream of the assumed autocatalytic activation). In such a case, we argue that the spikes of the total Arp2/3 complex concentration would occur in between those of barbed ends (or activator) and those of F-actin. We find however that the simulated time delay between peaks of Arp2/3 complex concentration and F-actin concentration is shorter by ~ 14% of the oscillation period compared to the time delay measured experimentally in Fig. 4 *D* in the main text. This indicates that the Arp2/3 complex may have a more direct role in the proposed autocatalytic amplification mechanism.

If we assume that the activator *A* recruits the Arp2/3 complex, we describe the concentration of Arp2/3 complex within the actin network in a manner similar to Eq. (2) of the main text:

$$\frac{\partial P}{\partial t} = k_P^+ A - k_P^- P \approx \left(\frac{k_B^- k_P^+}{k_B^+} \right) B - k_P^- P\,, \tag{S14}$$

after using $B \approx \frac{k_B^+ A}{k_B^-}$, see discussion preceding Eq. (4). Here P denotes the concentration of Arp2/3 complex associated with the actin meshwork and k_P^+ and k_P^- govern the rates of branch nucleation and Arp2/3 complex dissociation by debranching, respectively.

Existing literature provides us with estimates of the the Arp2/3 complex rate constants. Measurement of lifetimes of single Arp2/3 complex subunits within the actin network indicated k_P^- = 0.048 s^{-1} (1). The average Arp2/3 complex-mediated nucleation rate has been estimated to be 0.11µM s^{-1} (9). Assuming, as in the main text, an average barbed end concentration of approximately 0.4 µM, we estimate $k_B^- k_P^+ / k_B^+ \approx 0.28$ s^{-1}.

Given the above estimates of the rate constants, we used Eq. (S14) to calculate the time-depedent concentration of bound Arp2/3 complex concentration from the concentration of barbed ends calculated by the model of Eq. (1)-(4). We provide an example of the bound Arp2/3 complex concentration predicted by this model in Fig. S10 *A*. This figure shows that spikes of free barbed end concentration precede those of Arp2/3 complex, which in turn precede those of F-actin. To measure the relative timing of various concentration changes, auto- and cross-correlation functions were calculated in Fig. S10 *B*, similarly to the curves in Fig. 3 *F* and 4 *D* in the main text. From these calculations we find that spikes in concentration of free barbed ends precede spikes in bound Arp2/3 complex by an average time $\tau_{B\text{-}P}$ = 10 s. We measure an average time delay between peaks in of Arp2/3 complex and spikes of F-actin concentration of $\tau_{P\text{-}F}$ = 8 s. This value of $\tau_{P\text{-}F}$ is smaller by 14% of the period compared to the time delay we would anticipate from experiment (the time delay $\tau_{P\text{-}F}$ in Fig. 4 *D* is 35 s for a cell with period 180 s; the period in the simulation was 130 s so the expected $\tau_{P\text{-}F}$ is ~ 25 s).

The time delays of the preceding paragraph depend mainly on k_P^-. Consider the response of the Arp2/3 complex concentration to changes in the activator concentration as a perturbation to the steady state (A^*, P^*). In Section 2 of the Supplementary Materials we showed that the system exhibits underdamped oscillatory response to sufficiently small perturbation for the parameter set from Table 1. Thus, for small damping, the peaks in *P* will trail peaks in *A* by a phase difference φ:

$$A(t) = A^* + \delta A^* e^{i\omega t}, \tag{S15}$$

$$P(t) = P^* + \delta P^* e^{i(\omega t - \phi)}. \tag{S16}$$

Here ω denotes the angular frequency of the oscillations. Substituting in Eq. (S14), we find that the phase difference depends on the angular frequency and the debranching rate, but not on k_P^+:

$$\tan\phi = \frac{\omega}{k_P^-}. \tag{S17}$$

From this an estimate of the phase offset can be calculated as a function of the off-rate k_P^-.

Simulations of the model are in agreement with the k_P^--dependent phase difference in Eq. S17, which corresponds to the time delay $\tau_{B\text{-}P}$. Fig. S10 *C* displays how $\tau_{B\text{-}P}$ and $\tau_{P\text{-}F}$ vary with the Arp2/3 complex off-rate, k_P^-. We find that increases in k_P^- lead to decreases in $\tau_{B\text{-}P}$. As well, we find that increases in k_P^- result in increases in $\tau_{P\text{-}F}$ (the reason is that we assumed that the delay between peaks of free barbed end concentration and peaks of the F-actin concentration, $\tau_{B\text{-}F}$, is independent of k_P^- and $\tau_{B\text{-}F} = \tau_{B\text{-}P} + \tau_{P\text{-}F}$). Fig. S10 *C* demonstrates that matching $\tau_{P\text{-}F} \approx 0.2\tau$ of Fig. 4 *D* in the main text requires a $k_P^- > 0.1$ s^{-1}, much faster than k_P^- = 0.048 s^{-1} (1). It is likely, therefore, that Arp2/3 complex does not passively follow activator dynamics, as modeled in Eq. S10, but is itself part of the activation mechanism (based on the assumptions of our model).

4. Comparison to Previous Theoretical Studies

We focus on actin dynamics during protrusion and retraction in the lamellipodium, unlike other models of lamellipodia that looked at steady state properties (10-15). In the main text we compare our work to those of Hecht *et al.* (16) and Xiong *et al.* (17) who modeled pseudopodia formation in *Dictyostelium* as an excitable system.

Our model has similarities to models of traveling actin waves and patches in the interior of *Dictyostelium* and neutrophils cells by Weiner *et al.* (18), Doubrovinski and Kruse (19), Whitelam *et al.* (20) and Carlsson (21). Most of these models ascribe the propagation of the F-actin structure to the diffusion of an actin nucleation promoting factor. The activator promotes individual actin filament growth and branching events. The resulting growth of the F-actin causes delayed inhibition and removal of the activator. Our model suggests that related mechanisms to those in actin waves may also play a role in lamellipodia.

Enculescu *et al.* (22) modeled the I and V protrusion and retraction patterns observed in PtK1, epithelial cells and MEFs adhered to a substrate. The protrusions and retractions of the XTC cell in Fig. 1 *H* are reminiscent of the V patterns, though the V shapes are less pronounced as compared to (23). We modeled this pattern as a system with underdamped linear relaxation kinetics (Fig. 3E that corresponds to Case III in Fig. S7, see also Fig. S9). We found that systems with parameter values corresponding to undamped oscillations (Case II in Fig. S7) exhibit I state patterns, i.e. coherent oscillation across the cell circumference. These V to I transitions result from different underlying biological mechanisms compared to that in (22). Enculescu et al. attributed protrusion and retraction to different fractions of filaments attached to the cell membrane while the concentration of barbed ends was constant. Our model, by contrast attributes importance to the changing number of barbed ends. Which of the two mechanisms dominates? The changing concentration of Arp2/3 complex (see Fig. 4 *B*) supports our model. Also, the mechanism in (22) suggests that the protrusion rate is approximately proportional to the polymerization rate (a relationship we did not explicitly model). However, polymerization rate and protrusion may be out of phase (see Discussion). We note that an extension of the model in (22) to include actin filament nucleation and capping (24) generates oscillations in both velocity and free barbed concentration. Future studies may help distinguish between the relative importance of membrane filament attachment and new barbed generation in protrusion and retraction dynamics.

Wolgemuth (25) proposed a coarse-grained mechanical model of leading edge protrusion and retraction, approximating the lamellipodial actin network as a 1-dimensional gel extending into the cell. He included stick-slip adhesion interactions with the substrate. In this model, lamellipodial growth during protrusion leads to rising stress. Contraction is triggered once a stress threshold is reached. This model does not require a self-recruiting activation process to galvanize F-actin assembly. While this model may capture the biophysics of the protrusion and retraction patterns that arise from changes in leading edge contraction (26-28), in our system the rate of retrograde flow is approximately constant. We also provided evidence suggesting feedbacks involving changes in actin polymerization kinetics.

Other models accounting for the actin meshwork as a contractile fluid, have been developed by Alt and Dembo (29) and Kuusela and Alt (30). In these models protrusion results from membrane disconnection from the actin meshwork followed by membrane expansion, driven by solvent flow. Protrusion ceases when the F-actin accumulates in the vicinity of the lamellipodium tip. This leads to F-actin accumulation following the initiation of protrusion events. This sequence of events could be consistent with our observations. Future experiments may be able to determine if the initial stages of protrusion are driven by actin polymerization, or by osmotic pressure, as suggested by Alt and co-workers.

Models by Gov and co-workers on cell-shape changes emphasize the role of curvature-sensing membrane-bound proteins (31-34). Gov and Gopinathan present a model in which membrane proteins diffuse along the membrane and locally activate actin polymerization (31). An elastic cell membrane deforms in response to protrusive forces generated by the induced actin polymerization, and the resulting deformation may recruit more membrane proteins. This could be the origin of the autocatalytic mechanism assumed in our model. Proteins with negative spontaneous curvature generate static sinusoidal patterns along the membrane. Shlomovitz and Gov found that addition of myosin-induced contraction to the model of (31) leads to membrane protrusions that travel as waves along the membrane (32). Thus, each point along the membrane undergoes rounds of protrusion and retraction. Here, we suggest a mechanism for that does not rely on periodic changes in myosin contraction (the latter should cause changes in retrograde flow rate). We also do not rely specifically on membrane curvature. The origin of the proposed feedback mechanisms may involve other components, in addition to curvature.

The role of signaling molecules in leading edge protrusion and retraction has not been considered extensively in modeling studies. Cirit et al.(35) proposed a model that included feedbacks between Rac-mediated membrane protrusion and rapid turnover of nascent adhesions, and myosin-dependent maturation of adhesions that inhibit protrusion. Simulations reproduced the extracellular matrix-dependent protrusions and retractions. Similarly to our model, protrusions and retractions were generated by a combination of feedback loops. This model focused on myosin and protrusion velocity as independent variables while here we emphasized actin dynamics. Despite these differences, the negative feedback by focal adhesions assumed in Cirit et al. (35) may correspond to our assumed actin-dependent inhibition and Rac may correspond to the activator in our model.

References

1. Miyoshi, T., T. Tsuji, …, and N. Watanabe. 2006. Actin-turnover dependent fast dissociation of capping protein in the dendritic nucleation actin network: evidence of frequent filament severing. J. Cell Biol. 175:947-955.
2. Smith, M. B., H. Li, T. …, and D. Vavylonis. 2010. Segmentation and tracking of cytoskeletal filaments using open active contours. Cytoskeleton. 67: 693–705.
3. Dubin-Thaler, B. J., G. Giannone, …, and M. P. Sheetz. 2004. Nanometer Analysis of Cell Spreading on Matrix-Coated Surfaces Reveals Two Distinct Cell States and STEPs. Biophys. J. 86:1794-1806.
4. Smith, M. B., E. Karatekin, …, and D. Vavylonis. 2011. Interactive, Computer-Assisted Tracking of Speckle Trajectories in Fluorescence Microscopy: Application to Actin Polymerization and Membrane Fusion. Biophys. J. i 101:1794-1804.
5. Watanabe, N., and T. J. Mitchison. 2002. Single-Molecule Speckle Analysis of Actin Filament Turnover in Lamellipodia. Science. 295:1083-1086.

6. Koestler, S. A., K. Rottner, …, and J. V. Small. 2009. F- and G-Actin Concentrations in Lamellipodia of Moving Cells. PLoS One 4:e4810.
7. Abraham, V. C., V. Krishnamurthi, …,and F. Lanni. 1999. The Actin-Based Nanomachine at the Leading Edge of Migrating Cells. Biophys. J. 77:1721-1732.
8. Schaub, S., J. J. Meister, and A. B. Verkhovsky. 2007. Analysis of actin filament network organization in lamellipodia by comparing experimental and simulated images. J. Cell Sci. 120:1491--1500.
9. Tsuji, T., T. Miyoshi, C…, and N. Watanabe. 2009. An Order of Magnitude Faster AIP1-Associated Actin Disruption than Nucleation by the Arp2/3 Complex in Lamellipodia. PLoS One 4:e4921.
10. Mogilner, A., and L. Edelstein-Keshet. 2002. Regulation of Actin Dynamics in Rapidly Moving Cells:A Quantitative Analysis. Biophys. J. 83:1237-1258.
11. Atilgan, E., D. Wirtz, and S. X. Sun. 2006. Mechanics and Dynamics of Actin-Driven Thin Membrane Protrusions. Biophys. J. 90:65-76.
12. Schaus, T. E., E. W. Taylor, and G. G. Borisy. 2007. Self-organization of actin filament orientation in the dendritic-nucleation/array-treadmilling model. Proc. Natl. Acad. Sci. U. S. A. 104:7086-7091.
13. Huber, F., J. Käs, and B. Stuhrmann. 2008. Growing Actin Networks Form Lamellipodium and Lamellum by Self-Assembly. Biophys. J. 95:5508-5523.
14. Schreiber, C. H., M. Stewart, and T. Duke. 2010. Simulation of cell motility that reproduces the force-velocity relationship. Proc. Natl. Acad. Sci. U. S. A. 107:9141-9146.
15. Michalski, P. J., and A. E. Carlsson. 2010. The effects of filament aging and annealing on a model lamellipodium undergoing disassembly by severing. Phys. Biol. 7:026004.
16. Hecht, I., D. A. Kessler, and H. Levine. 2010. Transient localized patterns in noise-driven reaction-diffusion systems. Phys. Rev. Lett. 104:158301.
17. Xiong, Y., C.-H. Huang, …, and P. N. Devreotes. 2010. Cells navigate with a local-excitation, global-inhibition-biased excitable network. Proc. Natl. Acad. Sci. U. S. A. 107:17079-17086.
18. Weiner, O. D., W. A. Marganski, …, and M. W. Kirschner. 2007. An actin-based wave generator organizes cell motility. PLoS Biol. 5:e221.
19. Doubrovinski, K., and K. Kruse. 2008. Cytoskeletal waves in the absence of molecular motors. Europhys. Lett. 83:18003.
20. Whitelam, S., T. Bretschneider, and N. J. Burroughs. 2009. Transformation from spots to waves in a model of actin pattern formation. Phys Rev Lett 102:198103.
21. Carlsson, A. E. 2010. Dendritic actin filament nucleation causes traveling waves and patches. Phys. Rev. Lett. 104:228102.
22. Enculescu, M., M. Sabouri-Ghomi, …, and M. Falcke. 2010. Modeling of protrusion phenotypes driven by the actin-membrane interaction. Biophys. J. 98:1571-1581.
23. Machacek, M., and G. Danuser. 2006. Morphodynamic profiling of protrusion phenotypes. Biophys. J. 90:1439-1452.
24. Faber, M., M. Enculescu, and M. Falcke. 2010. Filament capping and nucleation in actin-based motility. Euro. Phys. J. Special Topics 191:147-158.
25. Wolgemuth, C. W. 2005. Lamellipodial Contractions during Crawling and Spreading. Biophys. J. 89:1643-1649.
26. Ji, L., J. Lim, and G. Danuser. 2008. Fluctuations of intracellular forces during cell protrusion. Nat. Cell Biol. 10:1393-1400.

27. Burnette, D. T., S. Manley, …, and J. Lippincott-Schwartz. 2011. A role for actin arcs in the leading-edge advance of migrating cells. Nat. Cell Biol. 13:371-382.
28. Giannone, G., B. J. Dubin-Thaler, …, and M. P. Sheetz. 2004. Periodic lamellipodial contractions correlate with rearward actin waves. Cell. 116:431-443.
29. Alt, W., and M. Dembo. 1999. Cytoplasm dynamics and cell motion: two-phase flow models. Math. Biosci. 156:207-228.
30. Kuusela, E., and W. Alt. 2009. Continuum model of cell adhesion and migration. Journal of Mathematical Biology 58:135-161.
31. Gov, N. S., and A. Gopinathan. 2006. Dynamics of Membranes Driven by Actin Polymerization. Biophys. J. 90:454-469.
32. Shlomovitz, R., and N. S. Gov. 2007. Membrane Waves Driven by Actin and Myosin. Phys. Rev. Lett. 98:168103.
33. Veksler, A., and N. S. Gov. 2007. Phase Transitions of the Coupled Membrane-Cytoskeleton Modify Cellular Shape. Biophys. J. 93:3798-3810.
34. Peleg, B., A. Disanza, …, and N. Gov. 2011. Propagating Cell-Membrane Waves Driven by Curved Activators of Actin Polymerization. PLoS One 6:e18635.
35. Cirit, M., M. Krajcovic, …, and J. M. Haugh. 2010. Stochastic Model of Integrin-Mediated Signaling and Adhesion Dynamics at the Leading Edges of Migrating Cells. PLoS Comput. Biol. 6:e1000688.

Table S1. Model Parameters

Parameter	Physical Meaning	Value
F_s	F-actin saturation concentration	200 μM [a]
k_F^+	Effective actin assembly rate	66 s^{-1} [b]
k_F^-	Effective actin disassembly rate	0.01s^{-1} [c]
k_A^-	Activator deactivation rate	0.03 s^{-1} [a]
D_A	Activator diffusion coefficient	0.1μm^2 s^{-1} [d]
r_0	Activation rate constant	5 μM s^{-1} [a]
r_2	Nonlinear activation rate constant	60 μM^{-1} s^{-1} [a]
L	Membrane Length	40 μm [e]
s_0	Noise Coefficient	0.02 μM μm$^{1/2}$ s$^{-1/2}$ [f]

[a] Values for these four rate constants were calculated based on four conditions (see SI Text): (i) the average F-actin concentration is between 500-1500μM (6-8); (ii) the average barbed end concentration is ~ 0.4 μM M; (iii) the system is in an excitable region with underdamped oscillations; (iv) the period of the oscillations is ~ 130 sec, as observed experimentally.

[b] A value 66 subunits/s was estimated in (1).

[c] Value chosen close to the inverse of time required for an actin subunit to traverse the lamellipodium by retrograde flow, $d_{\mathrm{lam}} / v_{\mathrm{retro}} \approx 100\,\mathrm{s}$, where $v_{\mathrm{retro}} \approx 50\,\mathrm{nm/s}$ is typical retrograde flow speed under our conditions, and $d_{\mathrm{lam}} \approx 5\,\mu\mathrm{m}$ is typical lamellipodium width. We note that single actin-GFP speckles in the lamellipodium disassemble at a rate ~ 0.03 s^{-1} (5). This faster rate likely includes remodeling processes within the lamellipodium that are not explicitly addressed in the present model.

[d] Value chosen to be similar to typical diffusion coefficients of proteins in eukaryotic cell membrane, but fit specifically to match the width of the spatial correlation function in Fig. S3 *B*.

[e] Length similar to arc length of membrane imaged experimentally.

[f] Value chosen to reproduce noise-induced excitations with a rate similar to the experiments of Fig. 1.

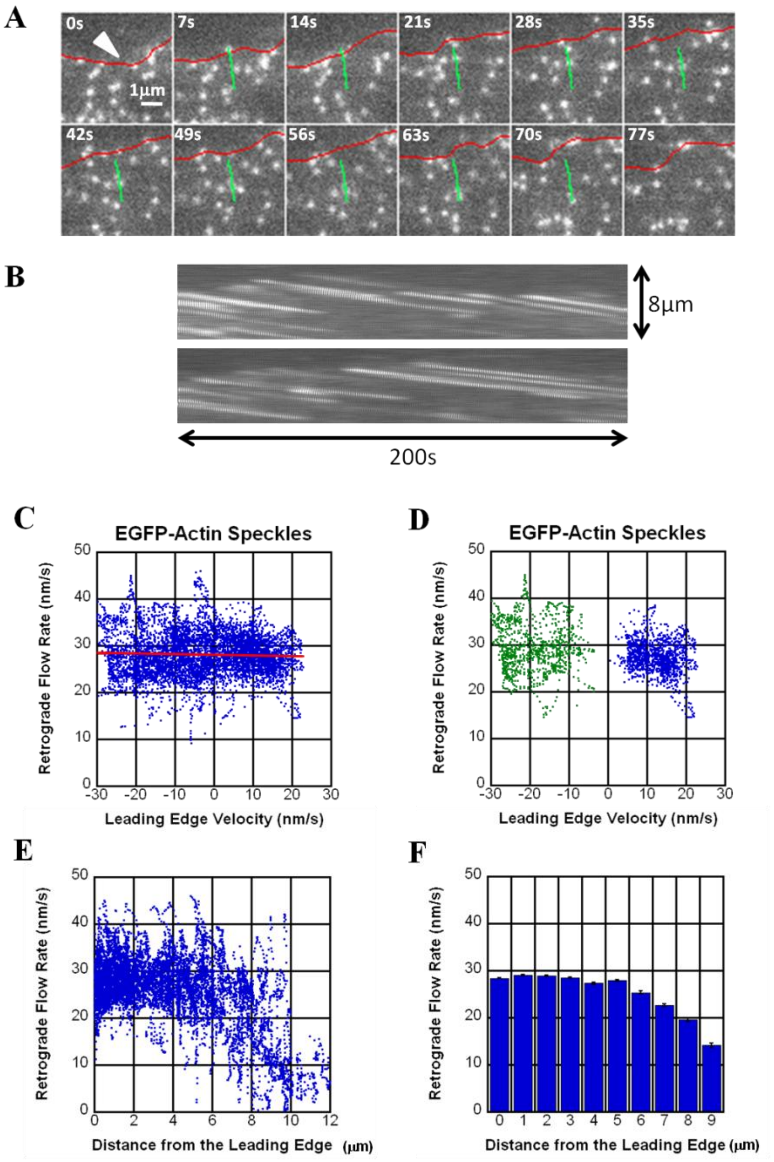

Figure S1. Single molecule fluorescent speckle microscopy measurements of retrograde flow rate for actin speckles. (A) EGFP-actin speckles from Fig. 1 *E* (1 frame/s, 200 s total). White arrow indicates site of speckle appearance. Speckle trajectory is shown in green during speckle lifetime. The tracked position of the leading edge is shown in red. (B) Kymographs of EGFP-actin speckles from Fig. 1 *E*. Individual speckle trajectories appear linear, suggesting a constant rate of retrograde flow over time. (C) Measurements of retrograde flow rates of EGFP-actin speckles from the cell in Fig. 1 *C*, as a function of leading edge speed. We included velocity measurements for all speckles that could be tracked. The graph includes measurements of velocity for the same speckles over each frame for which velocity calculation was possible. Line of best fit, shown in red, has negative slope 0.016, indicating a less than 2% change in retrograde flow compared to leading edge speed, on average. Similar results were obtained by analysis of a 400 s movie at 0.5 frame/s. (D) Measurements of retrograde flow rates of EGFP-actin speckles, as in panel B, however speckles were selected from regions visibly protruding (blue) or retracting (green). The separation between the data points indicates that regions of the cell whose leading edge velocity differ by 30 nm/s present retrograde flow rates which differ by less than 5 nm/s. (E) Retrograde flow rates of EGFP-actin speckles from the cell in Fig. 1 *C*, as a function of distance from the leading edge. (F) Average retrograde flow rates of EGFP-actin speckles from the cell in Fig. 1 *C*, as a function of distance from the leading edge. Error bars are standard error of the mean.

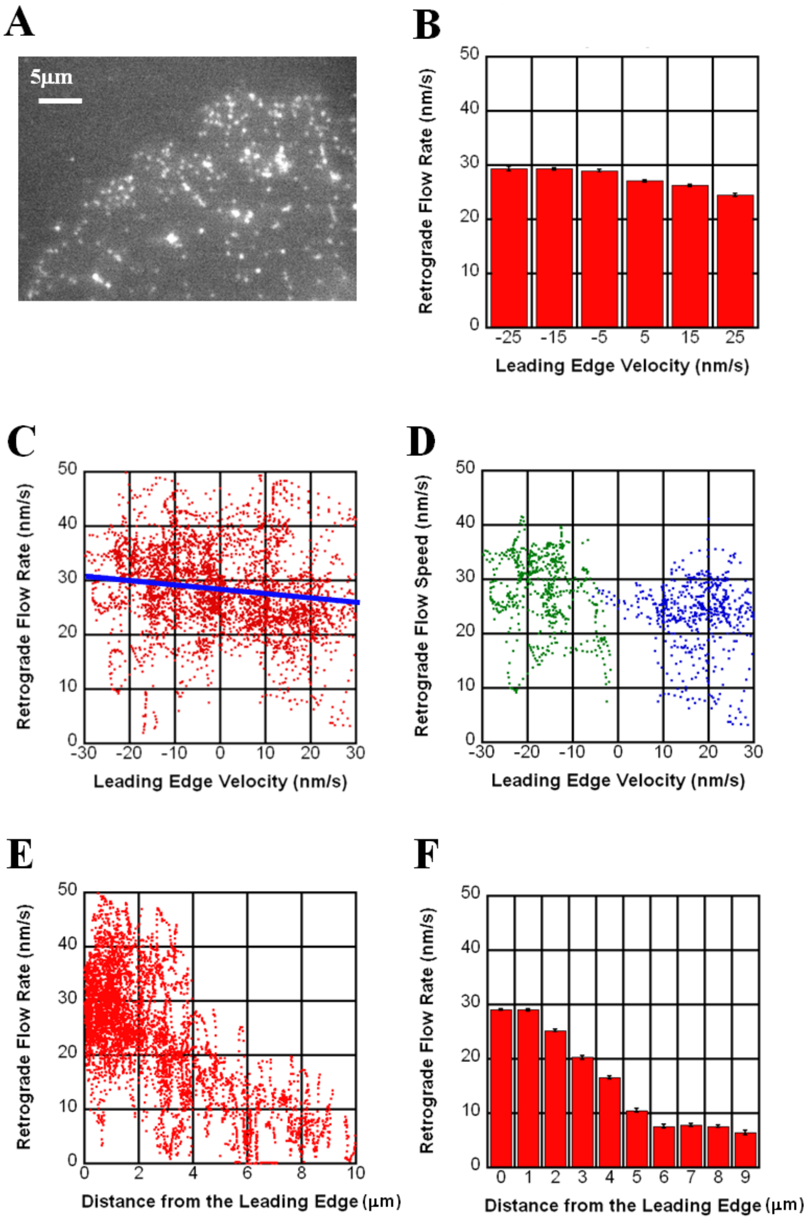

Figure S2. Single molecule fluorescent speckle microscopy measurements of retrograde flow rate with EGFP-p21 (A) XTC cell expressing EGFP-p21 at low concentration (1 frame/s, 200 s total). (B) Average retrograde flow rates of EGFP-p21 speckles from the cell in panel A, as a function of leading edge speed. Error bars are standard error of the mean. (C) Measurements of retrograde flow rates of EGFP-p21 speckles from the cell in panel A, as a function of leading edge speed. We included velocity measurements for all speckles that could be tracked. The graph includes measurements of velocity for the same speckles over each frame for which velocity calculation was possible. Line of best fit, shown in red, has negative slope 0.086, indicating a less than 10% change in retrograde flow compared to leading edge speed, on average. Similar results were obtained by analysis of a 160 s movie at 0.5 frame/s. (D) Measurements of retrograde flow rates of EGFP-p21 speckles, as in panel C, however speckles were selected from regions visibly protruding (blue) or retracting (green). The separation between the data points indicates that regions of the cell whose leading edge velocity differ by 30 nm/s present retrograde flow rates which differ by less than 5 nm/s. (E) Retrograde flow rates of EGFP-p21 speckles from the cell in panel A, as a function of distance from the leading edge. (F) Average retrograde flow rates of EGFP-p21 speckles from the cell in panel A, as a function of distance from the leading edge. Error bars are standard error of the mean.

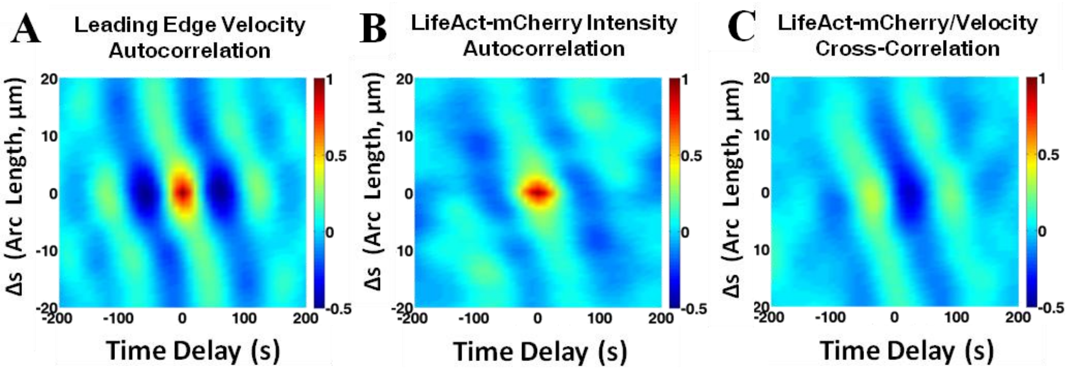

Figure S3. Two-Dimensional correlation functions of leading edge velocity and LifeAct-mCherry intensity (for cell in Fig. 1G of the main text). (A) Average autocorrelation coefficients for leading edge velocity vs. arc length and time indicate periodicity and wave-like propagation. Here, arc-length is calculated by multiplying angular positions in Figs. 1 *H* and *I* by a constant cell radius. The diagonal stripe patterns reflect the wave-like propagation of protrusion and F-actin assembly suggested by Fig. 1 *H* and *I*. Because of the random direction of propagation, the direction of the tilt of the stripes depends on the dominant wave feature in the movie. In some cells, this is found to be in the opposite direction as compared to panel *A* while others do not show any diagonal features. (B) Average autocorrelation coefficients for LifeAct-mCherry intensity within the first 5μm of the leading edge, as a function of position and time. The pattern is similar to panel A. (C) The cross-correlation coefficients between LifeAct-mCherry intensity and leading edge velocity vs. position and time. The cross-correlation has a minimum near the origin, indicating that velocity and actin dynamics are almost exactly out of phase.

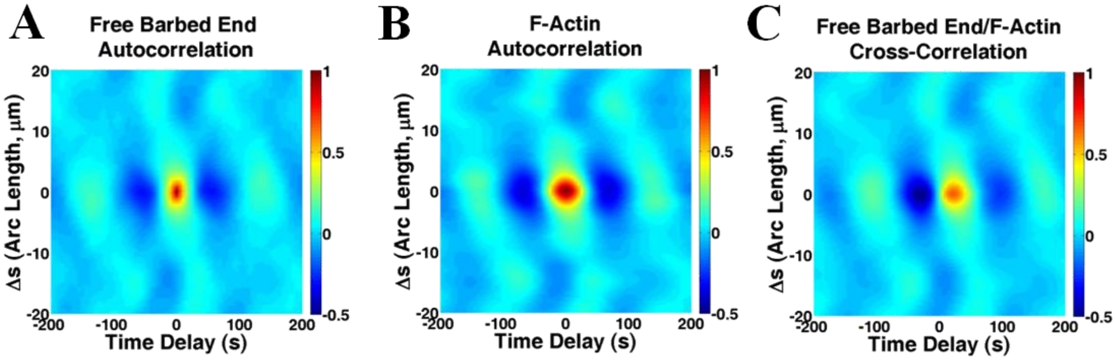

Figure S4. Two-Dimensional correlation functions of free barbed end concentration and F-actin concentration (for simulation in Fig. 3 of the main text). (A) Average autocorrelation coefficients for free barbed end concentration from Fig. 3D in the main text, as a function of arc length and time. The diagonal striping indicates diffusive propagation of free barbed ends along the membrane. (B) Same as panel A, for F-actin of Fig. 3E in the main text. (C) Average cross-correlation coefficients between free barbed ends and F-actin vs. arc length and time. The position of the largest peak to the right of the origin indicates that the free barbed end concentration spikes precede those of F-actin.

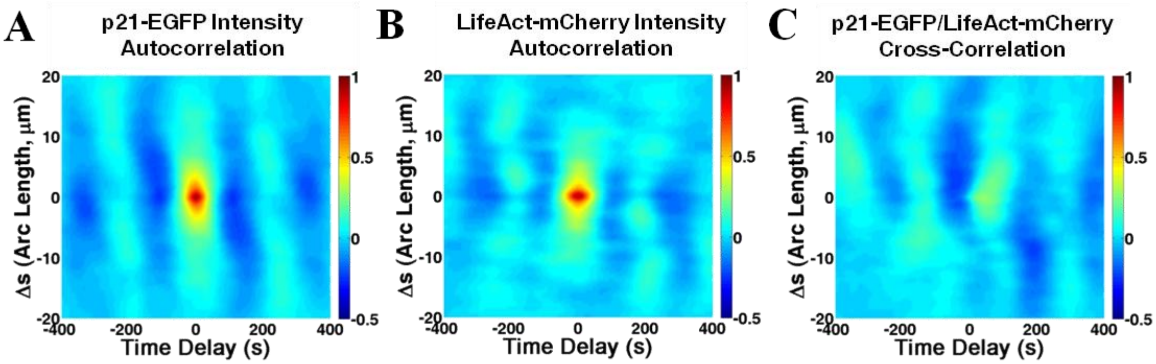

Figure S5. Two-Dimensional correlation functions of p21-EGFP intensity and LifeAct-mCherry intensity (for cell in Fig. 4 of the main text). (A) Average autocorrelation for p21-EGFP intensity for the cell in Fig. 4A in the main text, as a function of time and arc length. The diagonal striping indicates diffusive propagation of the Arp2/3 complex along the membrane. (B) Average autocorrelation for LifeAct-mCherry intensity as a function of time and arc length. (C) Average cross-correlation for p21-EGFP and LifeAct-mCherry as a function of time and arc length.

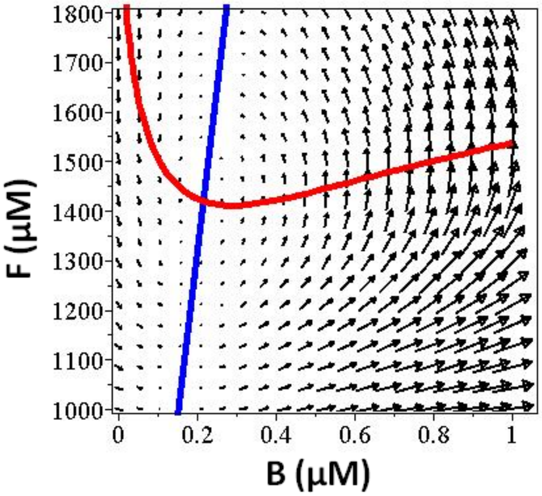

Fig. S6. Fixed points of the system . Phase plot of the concentration of *F* and B for the parameter set in Table 1. The nullclines *u*(*B*,*F*) = *0* and *v*(*B*,*F*)= *0* are shown in red and blue, respectively. The vector field indicates a flow towards the stable fixed point where the nullclines intersect. The trajectory of the vector field indicates that perturbations from the fixed point result in a spike of *A*, followed by a spike in *F*, before returning to the stable steady-state solution.

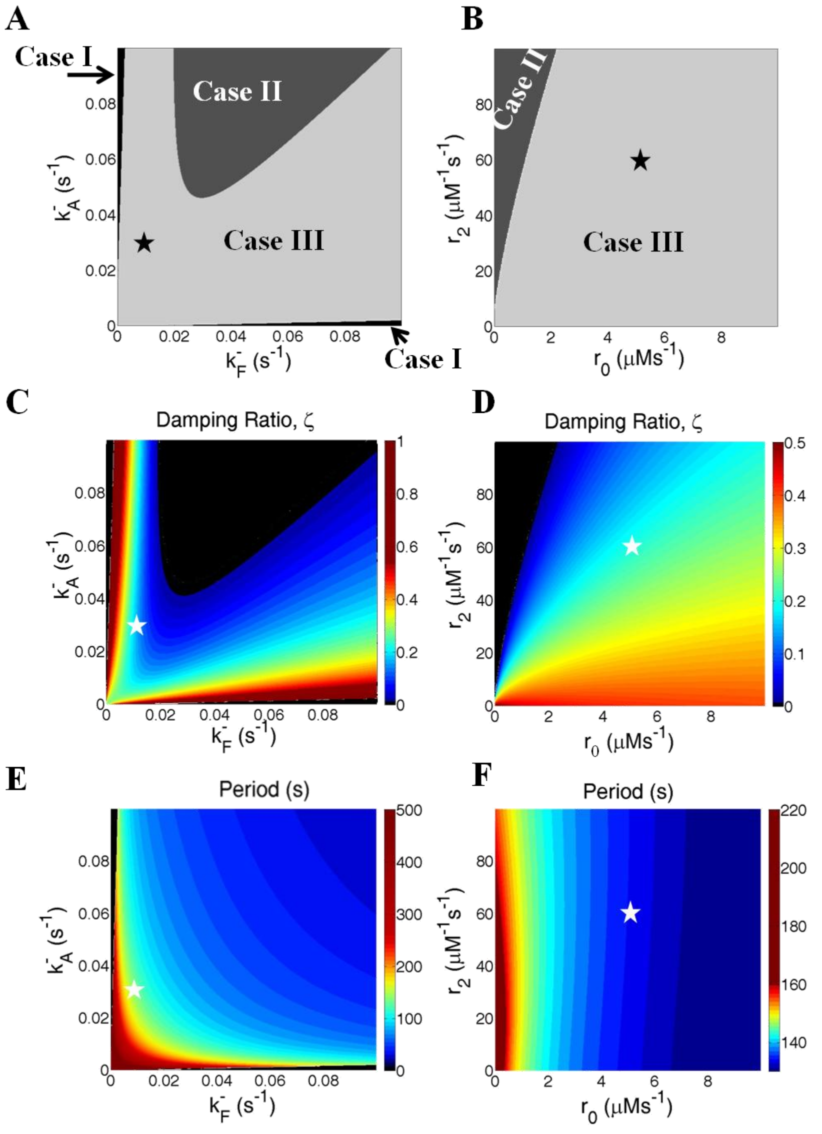

Figure S7. Stability analysis predicts characteristics of model solutions. (A) Results of linear stability analysis as function of k_F^- and k_A^- with other parameters as in Table 1, and with wave number q = 0. The exact point desccribed by Table 1 is indicated by the black star. Fixing all parameters and varying only one allows for switching between regions of parameter space. Case I (black): non-oscillatory solutions; Case II (dark gray): unstable oscillatory solutions; Case III (light gray): stable oscillatory solutions. (B) Same as panel A, as function of r_2 and r_0. (C,D) Damping ratio, calculated for regions of parameter space within Case III, for the parameter spaces shown in panels A, B. Regions of parameter space producing solutions for Case I or Case II are in black. The exact point desccribed by Table 1 is indicated by the white star. (E,F) Similar to panels C, D, but displaying period τ for both Case II and Case III solutions .

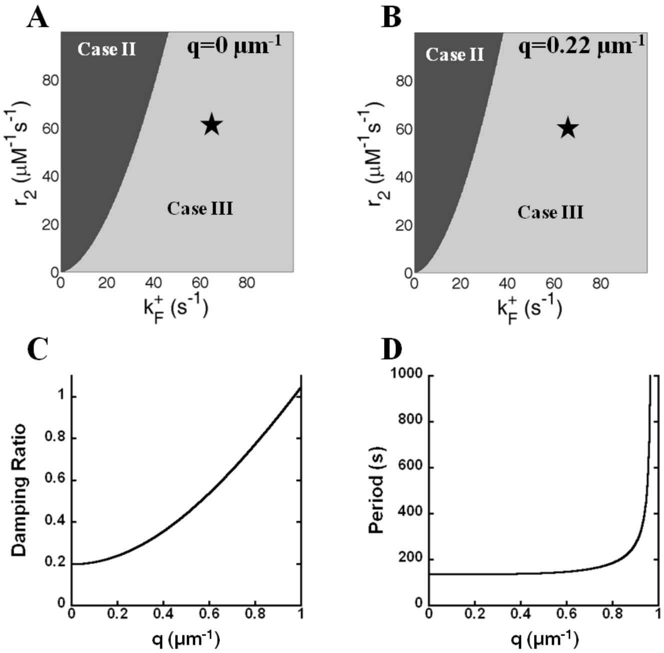

Figure S8. Dependence of results of stability analysis on wave-number, *q*. (A) Results of linear stability analysis as function of k_F^+ and r_2 with other parameters as in Table 1, and with wave number q = 0. The exact point desccribed by Table 1 is indicated by the black star. Fixing all parameters and varying only one allows for switching between regions of parameter space. Case I (black): non-oscillatory solutions; Case II (dark gray): unstable oscillatory solutions; Case III (light gray): stable oscillatory solutions. (B) Same as panel A, showing that with increasing wavenumber q the region of instability shrinks. (C) Damping ratio ζ for the parameter set in Table 1, as a function of wavenumber, q. The oscillations are more damped for larger q values, transitioning to overdamped solutions at $q \approx 0.97 \mu m^{-1}$ (D) Similar to panel C, but for period of oscillations, τ. The transition to a non-oscillatory solution at $q \approx 0.97$ μm^{-1} results in a rapid divergence of the period.

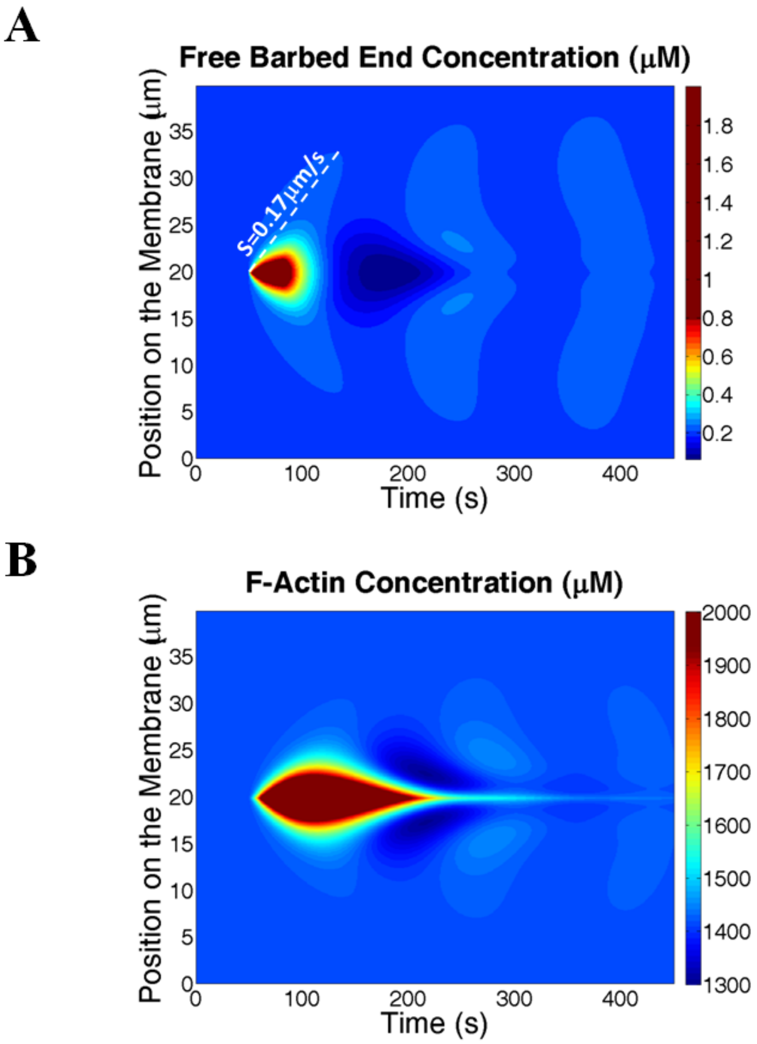

Figure S9. Simulated response of system to point excitation of a steady-state. We find similar tear-drop shapes to those of Hecht. et al (16), but less 'V' shaped compared to Enculescu et al. (22). (A) Free barbed end concentration, generated by localizing noise, $s(t)$ = 0.1 μM s^{-1}, at a single point (at 20 μm) along the membrane for 1.5 s. Simulations were run with the parameters from Table S1, except the noise term, which was zero outside the region described above. Excitations spread from the region at which noise was applied with a speed of approximately 0.17 μm/s. This is similar to the speed of protrusion propagation in Fig. 1 *H*. In the presence of multiple sources of noise, in the model these excitations combine into transient wave-like patterns. (B) F-Actin concentration corresponding to the free barbed concentration shown in panel A.

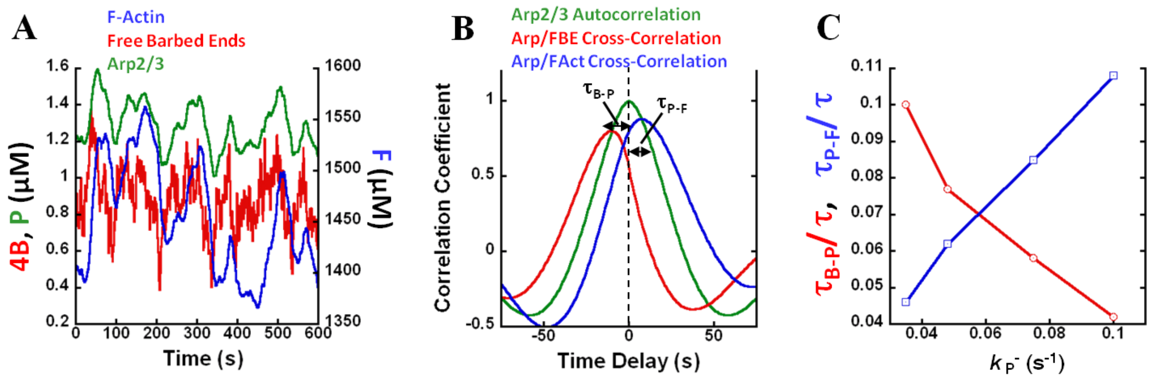

Fig. S10. Model of Arp2/3 complex concentration, compared to free-barbed end and F-actin concentrations. (A) Model-generated barbed end concentration *B* (red, multiplied by a factor of 4), and F-actin *F* (blue) vs time. Data generated using the parameters in Table 1. The concentration of Arp2/3 complex, *P*, was calculated from Eq. (S10) with $k_B^- k_P^+ / k_B^+ = 0.028 s^{-1}$ and $k_P^- = 0.048 s^{-1}$. Spikes of *P* (green) follow spikes in *B*, but precede spikes in *F*. (B) The correlation functions of the data from panel A, including the auto-correlation of *P* (green), cross-correlation of *P* with *B* (red), and cross-correlation of *P* with *F* (blue). The relative offsets of the cross-correlation peak indicates that, on average, spikes in *B* precede spikes in *P* by $\tau_{B\text{-}P}$ = 10 s, while spikes in *P* precede spikes in *F* by $\tau_{P\text{-}F}$ = 8 s. (C) The fractional offsets $\tau_{B\text{-}P}/\tau$ and $\tau_{P\text{-}F}/\tau$ vary with changes in the *P* off-rate, k_P^-, consistent with Eq. (S13).

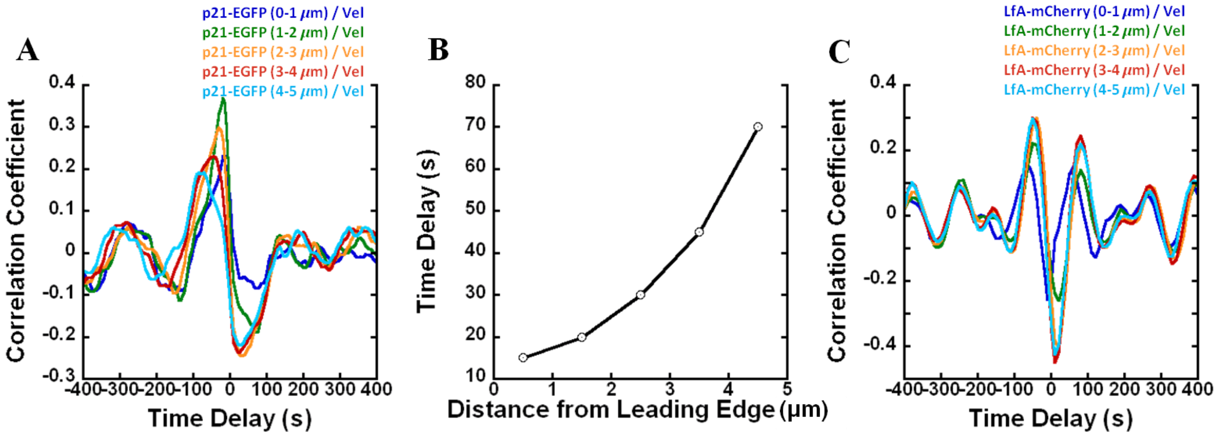

Figure S11. Spatial dependence of Arp2/3 complex and LifeAct correlation with leading edge velocity. (A) Cross-correlation of p21-EGFP intensity with leading edge velocity for the cell in Fig. 4 *A*. The p21-EGFP intensity was measured in ribbons of width 1 μm at various distances from the leading edge of the cell. The maximum peaks of the cross-correlation functions occur at negative time delays, indicating that peaks in leading edge velocity precede peaks in Arp2/3 complex concentration. (B) The magnitude of the time delay calculated from the cross-correlation peaks in panel A increases with distance from the leading edge, suggesting that Arp2/3 complex at the leading edge closely follows changes in leading edge velocity, while there is a longer delay to coordination within the interior of the lamellipodium. (C) Cross-correlation of LifeAct-mCherry intensity with leading edge velocity for the cell in Fig. 1 *G*. The LifeAct-mCherry intensity was measured in ribbons of width 1 μm at various distances from the leading edge of the cell. LifeAct within 1 μm of the leading edge is less anticorrelated than the LifeAct in other regions. Unlike panel A for p21, we do not observe a clear trend for the time delay, likely because of many mechanisms that modify F-actin during a protrusion and retraction cycle.

Movies

Movie S1. XTC cell expressing LifeAct-EGFP at low concentrations. Cell has been on substrate for 100 min. Resolution is 80nm/pixel. Images acquired at 100ms/frame.

Movie S2. XTC cell expressing LifeAct-mCherry in Fig. 1A. Cell has been on substrate for 60min. Resolution is 160nm/pixel. Images acquired at 10s/frame.

Movie S3. XTC cell expressing LifeAct-mCherry in Fig. 1G. Cell has been on substrate for 40min. Resolution is 80nm/pixel. Images acquired at 10s/frame.

Movie S4. XTC cell expressing LifeAct-mCherry (red) and p21-EGFP (green) in Fig. 4. Cell has been on substrate for 180 min. Resolution is 80nm/pixel. Images acquired at 5s/frame.

Movie S5. XTC cell expressing LifeAct-mCherry (red) and p21-EGFP (green) in Fig. 5. Cell has been on substrate for 4 hours and is treated with fetal calf serum at frame 41. Resolution is 80nm/pixel. Images acquired at 5s/frame.